The modeled seasonal cycles of surface N_2O fluxes and atmospheric N_2O

Qing Sun[1,2], Fortunat Joos[1,2], Sebastian Lienert[1,2], Sarah Berthet[3], Dustin Carroll[4], Cheng Gong[5], Akihiko Ito[6,7], Atul K. Jain[8], Sian Kou-Giesbrecht[9,10], Angela Landolfi[11], Manfredi Manizza[12], Naiqing Pan[13,14], Michael Prather[15], Pierre Regnier[16], Laure Resplandy[17], Roland Séférian[3], Hao Shi[18], Parvadha Suntharalingam[19], Rona L. Thompson[20], Hanqin Tian[13,14], Nicolas Vuichard[21], Sönke Zaehle[5], Qing Zhu[22]

[1] Climate and Environmental Physics, Physics Institute, University of Bern, Bern, Switzerland

[2] Oeschger Centre for Climate Change Research, University of Bern, Bern, Switzerland

[3] CNRM, Université de Toulouse, Météo France, CNRS, Toulouse, France

[4] Moss Landing Marine Laboratories, San José State University, Moss Landing, California, USA

[5] Biogeochemical Signals Department, Max Planck Institute for Biogeochemistry, Jena, Germany

[6] Graduate School of Life and Agricultural Sciences, University of Tokyo, Tokyo, Japan

[7] Earth System Division, National Institute for Environmental Studies, Tsukuba, Japan

[8] Department of Atmospheric Sciences, University of Illinois, Urbana-Champaign, Urbana, IL61801, USA

[9] Department of Earth and Environmental Sciences, Dalhousie University, Halifax, NS, Canada

[10] Canadian Centre for Climate Modelling and Analysis, Environment and Climate Change Canada, Victoria, BC, Canada

[11] Institute of Marine Sciences, National Research Council (ISMAR-CNR), Via Fosso del Cavaliere 100, Rome, Italy

[12] Geosciences Research Division, Scripps Institution of Oceanography, University of California-San Diego, La Jolla, CA

[13] Schiller Institute for Integrated Science and Society, Department of Earth and Environmental Sciences, Boston College, Chestnut Hill, MA 02467, USA

[14] International Center for Climate and Global Change Research, College of Forestry, Wildlife and Environment, Auburn University, Auburn 36830, USA

[15] Department of Earth System Science, University of California Irvine, Irvine, CA, USA

[16] Department Geoscience, Environment & Society - BGEOSYS, Université Libre de Bruxelles, 1050-Brussls, Belgium

[17] Princeton University, Geosciences Department, High Meadows Environmental Institute, Princeton, NJ, USA

[18] State Key Laboratory of Urban and Regional Ecology, Research Center for Eco-Environmental Sciences, Chinese Academy of Sciences, Beijing 100085, China

[19] Centre for Ocean and Atmospheric Sciences, School of Environmental Sciences, University of East Anglia, NR4 7TJ, United Kingdom

[20] Climate and Environment Research Institute - NILU, 2007 Kjeller, Norway

[21] Laboratoire des Sciences du Climat et de l'Environnement, LSCE-IPSL (CEA-CNRS-UVSQ), Université Paris-Saclay 91191 Gif-sur-Yvette, France

[22] Climate and Ecosystem Sciences Division, Lawrence Berkeley National Lab, 1 Cyclotron Road, Berkeley, CA 94720, USA

Corresponding author: Qing Sun (qing.sun@unibe.ch)

Key Points:

- Model land biosphere and ocean surface fluxes are combined with tropospheric transport to simulate N_2O seasonality at six monitoring sites
- Surface N_2O fluxes contribute substantially to the observed seasonality of tropospheric N_2O, partly offsetting stratospheric contribution
- Large spread in seasonal land fluxes call for biosphere model improvements, e.g., using N_2O observations and transport-chemistry modeling

Abstract

Nitrous oxide (N_2O) is a greenhouse gas and an ozone-depleting agent with large and growing anthropogenic emissions. Previous studies identified the influx of N_2O-depleted air from the stratosphere to partly cause the seasonality in tropospheric N_2O (aN_2O), but other contributions remain unclear. Here we combine surface fluxes from eight land and four ocean models from phase 2 of the Nitrogen/N_2O Model Intercomparison Project with tropospheric transport modeling to simulate aN_2O at the air sampling sites: Alert, Barrow, Ragged Point, Samoa, Ascension Island, and Cape Grim for the modern and preindustrial periods. Models show general agreement on the seasonal phasing of zonal-average N_2O fluxes for most sites, but, seasonal peak-to-peak amplitudes differ severalfold across models. After transport, the seasonal amplitude of surface aN_2O ranges from 0.25 to 0.80 ppb (interquartile ranges 21-52% of median) for land, 0.14 to 0.25 ppb (19-42%) for ocean, and 0.13 to 0.76 ppb (26-52%) for combined flux contributions. The observed range is 0.53 to 1.08 ppb. The stratospheric contributions to aN_2O, inferred by the difference between surface-troposphere model and observations, show 36-126% larger amplitudes and minima delayed by ~1 month compared to Northern Hemisphere site observations. Our results demonstrate an increasing importance of land fluxes for aN_2O seasonality, with land fluxes and their seasonal amplitude increasing since the preindustrial era and are projected to grow under anthropogenic activities. In situ aN_2O observations and atmospheric transport-chemistry models will provide opportunities for constraining terrestrial and oceanic biosphere models, critical for projecting surface N_2O sources under ongoing global warming.

Plain Language Summary

Anthropogenic N_2O emissions, e.g., from fertilizer use on agricultural land, fossil fuel burning, and industrial activities, continue to increase atmospheric N_2O to values unprecedented for at least the past 800,000 years. This increase causes harmful global warming and stratospheric ozone depletion. Understanding how N_2O emissions from land and ocean influence atmospheric composition and climate is a research priority. Here, we address specifically how land and ocean emissions contribute to the seasonality of N_2O at six air monitoring sites. We apply surface N_2O fluxes simulated by eight land biosphere and four ocean biogeochemical models with a representation of lower atmosphere transport. This study complements earlier studies that show a strong influence on N_2O seasonality by the influx of N_2O-depleted air from the upper atmosphere. We demonstrate that land biosphere and ocean surface fluxes contribute substantially to the observed seasonal cycle at the different measurement sites. The surface contributions dampen the seasonal signal from the upper atmosphere and must be considered for explaining the observed N_2O seasonality. However, surface fluxes differ widely across models. In future work, atmospheric N_2O observations and transport modeling, considering both lower and upper atmospheric contributions, may help to better constrain biosphere models.

1 Introduction

Nitrous oxide (N_2O) is one of the main greenhouse gases [*Canadell et al.*, 2021; *Forster et al.*, 2021] and an ozone-depleting agent [*Crutzen*, 1970; *Ravishankara et al.*, 2009]. Its atmospheric mixing ratio (aN_2O) in the troposphere has increased from 271 ppb (parts per billion) since pre-industrial time to over 330 ppb in recent years (global average) [*Lan et al.*, 2023a; *MacFarling Meure et al.*, 2006]. The ice core records of aN_2O of the past 800,000 years [*Schilt et al.*, 2010] and recent reconstructions of N_2O emissions using aN_2O and isotope data of

ice cores show that anthropogenic contributions dominate this increase [*Fischer et al.*, 2019]. The application of synthetic fertilizers since the green revolution is one of the main reasons for the increase in N_2O emissions [*H Tian et al.*, 2019]. N_2O has an atmospheric lifetime of approximately 115 years [*Canadell et al.*, 2021; *Prather et al.*, 2015] before being removed in the stratosphere which leads to ozone depletion [*Crutzen*, 1970; *Mueller*, 2021]. Therefore, the unprecedented rise in N_2O emissions and aN_2O poses multiple threats to natural systems and our society [*IPCC*, 2021; 2022].

As N_2O is predominantly produced by microbes in soils and waters [*Bakker et al.*, 2014; *Butterbach-Bahl et al.*, 2013], N_2O emissions are largely affected by environmental conditions which are under the influence of the changing climate and anthropogenic activities. The long-term changes in N_2O emissions and tropospheric aN_2O have been studied and reported for glacial-interglacial variations [*Joos et al.*, 2020; *Rubino et al.*, 2019; *Schilt et al.*, 2010]. For the modern period, the N_2O emissions from terrestrial ecosystems and the oceans have been investigated progressively across scales with site observations [e.g., *Kock and Bange*, 2015; *Pastorello et al.*, 2020], field experiments [e.g., *Breider et al.*, 2019; *Dijkstra et al.*, 2012], as well as modeling [e.g., *Martins et al.*, 2022; *Landolfi et al.*, 2017; *Xu-Ri and Prentice*, 2008; *Manizza et al.*, 2012]. However, due to the complex processes of N_2O production in soils, inland waters and oceans [e.g., *Battaglia and Joos*, 2018; *Ma et al.*, 2022; *Hutchins and Capone*, 2022] and loss in the stratosphere [*Mueller*, 2021], there is still poor understanding of the controls on tropospheric aN_2O and its seasonal and inter-annual variations.

Since the seasonality of aN_2O has been detected with high-precision measurements [*Jiang et al.*, 2007], research on the seasonal and interannual net flux of stratosphere-troposphere exchange (STE) of N_2O has demonstrated its large impact on aN_2O seasonality [e.g., *Nevison et al.*, 2011; *D. J. Ruiz et al.*, 2021; *Daniel J. Ruiz and Prather*, 2022]. aN_2O was also inverted using atmospheric transport models to derive surface N_2O fluxes [e.g., *Bergamaschi et al.*, 2015; *Hirsch et al.*, 2006; *Thompson et al.*, 2019] which showed the importance of surface N_2O fluxes for aN_2O seasonality and interannual variability. As terrestrial ecosystems have been largely responding to climate and environmental changes, including the increasing atmospheric CO_2 concentration and enhanced N-fertilizer application [*Tian et al.*, 2020; *Walker et al.*, 2021], compared to pre-industrial time, the annual terrestrial emissions of N_2O have also increased in recent decades across the globe and with different intensities along the latitudinal zones (e.g., 2007-2016, see Figure 2 by *Tian et al.* [2020]). Due to the lack of global monthly anthropogenic N_2O emissions, some earlier studies could not consider the influence of the rising N_2O emissions from agriculture and natural terrestrial systems on aN_2O seasonality [*Nevison et al.*, 2005]. In contrast, more recent aN_2O inversion studies still typically used a limited set of N_2O surface flux estimates from ocean and land as priors [*Liang et al.*, 2022; *Patra et al.*, 2022; *Thompson et al.*, 2014]. Hence, information on how N_2O fluxes from land and ocean emissions, especially in the changing land biosphere, contribute to the seasonal variation in aN_2O is still lacking.

Therefore, to assess the human impacts on aN_2O, there is a need to understand the response of aN_2O to the rapidly rising terrestrial N_2O emissions. In this study, we analyze the seasonal variations in N_2O flux estimates from eight Terrestrial Biosphere Models participating in the global Nitrogen/N_2O Model Inter-comparison Project (NMIP [*Tian et al.*, 2018]) and four ocean biogeochemical models. The flux patterns from these models are prescribed in an atmospheric transport matrix to simulate their contribution to the aN_2O seasonality at a set of air monitoring stations.

2 Materials and Methods

2.1 N_2O emissions

The N_2O fluxes from the land and ocean were simulated separately as part of the Nitrogen/N_2O Model Intercomparison Project (NMIP-2) [*Tian et al.*, 2018]. The soil emissions of N_2O from terrestrial ecosystems, both natural and agricultural lands, were modeled with eight process-based Terrestrial Biosphere Models (TBMs) and air-ocean fluxes with four Earth system/ocean biogeochemical models (Table 1). As the analysis for spatial data was carried out at $0.5^o \times 0.5^o$ resolution, model outputs with different resolutions were regridded with a conservative remapping method. Natural fires and related biomass burning N_2O emissions are included in the TBM ensemble. Surface N_2O emissions from industry and fossil fuel (~1 TgN yr^{-1}), and from anthropogenic biomass burning, waste and wastewater, lightning, and inland and estuaries (~2 TgN yr^{-1}), totaling ca. 18 % of overall emissions (~17 TgN yr^{-1}) for the period 2007-2016, are not included (for detailed estimates of source contributions see *Tian et al.*, 2020]. These sectorial emissions (industry, fossil) are likely to have a comparably small influence on aN_2O seasonality at the six remote stations, given their small magnitude. All TBMs were forced with the same, NMIP-2, input datasets (Table 2). The climate data from 1901 to 1920 were recycled for the spin-up period and the 1850 to 1900 period of transient simulation. In addition, there is a control simulation for 171 years with recycled climate data from 1901 to 1920 and other forcing data fixed at the earliest available time (see Table 2). The control simulations show no drift in N_2O emissions, indicating an equilibrium state. Ocean emissions have a relatively small influence on modeled aN_2O seasonality (see results), and we refer to *Tian et al.*, 2020 and references in Tab. 1 for information on the 3-dimensional, dynamic ocean circulation-biogeochemistry models used to simulate ocean N_2O subsurface production from nitrification and denitrification and resulting net exchange with the atmosphere. The ocean-model emissions are compared to an observation-derived global climatology [*Yang et al.* 2020].

Table 1 Terrestrial Biosphere Models and ocean biogeochemical models for N_2O surface fluxes in the NMIP-2 ensemble and descriptions. N/A: not applicable; S/A: same as above.

Model	Reference	Resolution (degree)	Pre-industrial representation	Present-day representation
		Land fluxes		
CLASSIC	*Melton et al.* [2020]	0.5	N/A	2001-2020
DLEM	*Tian et al.* [2015]	0.5	1861-1880	S/A
ELM	*Zhu et al.* [2019]	0.5	S/A	S/A
ISAM	*Shu et al.* [2020]	0.5	S/A	S/A
LPX-Bern	*Lienert and Joos* [2018]	0.5	S/A	S/A
OCN	*Zaehle and Friend* [2010]	1	S/A	S/A
ORCHIDEE	*Vuichard et al.* [2019]	0.5	S/A	S/A
VISIT	*Ito et al.* [2018]	0.5	S/A	S/A
		Ocean fluxes		
Bern3D	*Battaglia and Joos* [2018]	ca. 8	S/A	2001-2020
UVic2.9	*Landolfi et al.* [2017]	$1.8^\circ \times 3.6^\circ$	N/A	2001-2019
CNRM-ESM2-1	*Seferian et al.* [2019]	0.25	N/A	2001-2018
ECCO-Darwin	*Carroll et al.* [2020], *Ganesan et al.* [2020]	1/3	N/A	2001-2013

Two periods were considered in this study, namely pre-industrial (PI) from 1861 to 1880, and present day (PD) from 2001 to 2020 or depending on the available model outputs (pre-industrial N_2O fluxes from the ocean are only available for Bern3D, Table 1). The intra-annual variations of the land and ocean N_2O fluxes were calculated by detrending the flux time series, i.e., monthly anomalies from 12-month running averages that are centered around zero by subtracting the overall mean.

Table 2 Input datasets for NMIP-2 Terrestrial Biosphere Models.

Input data	Source/product	Period	Reference
Climate	CRU-JRA55	1901-2020	*Harris* [2021]
Atmospheric CO_2	Ice core CO_2 data and NOAA annual observations	1850-2020	*Joos and Spahni* [2008]; *Lan et al.* [2023b]
Land cover change	Land-Use Harmonization (LUH2)	1850-2020	*Hurtt et al.* [2020]
Atmospheric nitrogen deposition	International Global Atmospheric Chemistry (IGAC)/Stratospheric Processes and Their Role in Climate (SPARC) Chemistry-Climate Model Initiative (CCMI)	1850-2020	*Hegglin et al.* [2016]
Nitrogen fertilization	Harmonized Anthropogenic Nitrogen Input (HaNi)	1911-2020	*Tian et al.*, 2022
Manure nitrogen	Harmonized Anthropogenic Nitrogen Input (HaNi)	1850-2020	*Tian et al.*, 2022

2.2 Modeled atmospheric N_2O anomaly

The local aN_2O seasonal cycles are simulated at six greenhouse gas monitoring stations, including two high-latitude stations (Alert and Barrow), three tropical stations (Ascension Island, Ragged Point, and Samoa), and one mid-latitude southern hemisphere station (Cape Grim). We use the Jacobian transport matrix determined by Kaminski et al. (1999) from a simulation with TM2, a global 3-dimensional model of the atmospheric transport of passive tracers [*Heimann*, 1995], The Jacobian matrix maps the influence of the surface flux from every grid cell and every month on aN_2O for a particular station and month. The matrix provides a convenient and cost-efficient way to quantify the basic impacts of surface fluxes on atmospheric tracer seasonality. *Kaminski et al. (1999)* applied TM2 with a horizontal resolution of $\sim 10^{o} \times 8^{o}$, 9 layers, a 4-hourly time step, and repeatedly cycling through the meteorological fields of the year 1987 from analyses of the European Center for Medium-Range Weather Forecast (ECMWF), adjusted for air mass conservation. Here, we use the transport matrix with surface N_2O fluxes from the previous 11 months and the current month when calculating the monthly aN_2O anomaly. Interannual variability in transport and its influence on aN_2O is not considered, while interannual aN_2O variability from surface flux variability is simulated. Stratospheric loss processes and the net flux of stratosphere-troposphere exchange (STE) on aN_2O seasonality are not represented by the TM2 matrix. Therefore, the simulated aN_2O seasonality from surface fluxes is expected to deviate from observations, given the importance of STE for aN_2O seasonality.

In the standard setup, monthly N_2O fluxes from the land by the TBMs and the ocean surface by ocean biogeochemical models (Table 1) in both PI and PD periods are the input for computing aN_2O anomalies. In addition, land and ocean emissions were passed separately to the TM2 matrix to assess their individual influence on aN_2O seasonality. Further, the impacts on

monthly aN_2O anomaly by the intra-annual variations in flux versus those from the deseasonalized spatial flux pattern were separately quantified. Accordingly, the detrended time series of N_2O fluxes from the land and ocean, i.e., monthly anomalies from 12-month running averages that are centered around zero by subtracting the overall mean, were used to simulate the aN_2O anomaly caused by the intra-annual variation of N_2O emissions. The 12-month running averages of the fluxes, as deseasonalized fluxes, were used to estimate the influence from the mean spatial pattern and long-term trend of N_2O emissions on aN_2O at each station. The sum of aN_2O simulated with these decomposed fluxes matches aN_2O simulated in the standard setup. For the total contribution from land and ocean surface flux to aN_2O seasonality, each individual land output was combined with every ocean output resulting 32 members for the total surface flux.

2.3 Atmospheric N_2O seasonality observations

The atmospheric N_2O mixing ratios (aN_2O) for the selected stations were obtained from surface flask measurements by National Oceanic and Atmospheric Administration (NOAA) Carbon Cycle Greenhouse Gases (CCGG) (www.esrl.noaa.gov/gmd/ccgg/obspack/) available at weekly to biweekly frequency [*Dlugokencky et al.*, 2021] (Table 5). Data for the selected stations were available from 2000-2001 to 2018-2019. Months with missing values were omitted. The observation-based seasonal aN_2O anomaly was calculated from the detrended time series, i.e., the difference from 12-month running averages then deducting the overall mean. The observation-based, period-mean seasonality of aN_2O is computed from the aN_2O anomalies weighted by the measurement uncertainties which are included in the datasets. The amplitude of aN_2O seasonality is determined as the min-to-max difference for each year.

2.4 Data analysis

The data analysis and plotting were carried out in Python [*Van Rossum and Drake Jr*, 1995] with packages xarray [*Hoyer and J. Hamman*, 2017], pandas [*The pandas development team*, 2020], and matplotlib [*Hunter*, 2007]. The seasonality of modeled N_2O fluxes and aN_2O is the temporal mean intra-annual variation over the investigated periods for each individual model and for the multi-model median. The seasonal amplitude of modeled N_2O fluxes and aN_2O is determined as the min-to-max difference of monthly fluxes or monthly mean mixing ratio on a yearly basis for each model. The multi-model median and quartiles of the seasonal amplitude are calculated from the long-term mean seasonal amplitudes of all the models as well as all the combinations of land and ocean models.

3 Results

3.1 Seasonality in modeled N_2O emissions

3.1.1 Land emissions

The multi-model medians of N_2O emissions show large intra-annual and spatial heterogeneity on land (red lines) and ocean (blue lines, Figure 1d, e, f). In austral summer (December, January, and February; DJF), high land emissions are simulated for the Southern Hemisphere (SH) in the tropics (0° – 20°S, 2.7 TgN yr^{-1}, multi-model median) and subtropics (20°S – 40°S, 0.85 TgN yr^{-1}, Figure 1a, d; Table 3) for the present-day period (PD; 2001-2020). Global average emissions for DJF (PI: 6.17 TgN yr^{-1}) grew 36% since the pre-industrial (PI,

1861-1880: 4.55 TgN yr^{-1}), with increases in all latitudinal zones (0.01 to 0.43 TgN yr^{-1}, Figure 1d; Table 3). In boreal summer (June, July, and August; JJA), high emissions are simulated for the Northern Hemisphere (NH) in the subtropics (20°N – 40°N, 3.62 TgN yr^{-1}), tropics (0° – 20°N, 2.78 TgN yr^{-1}), and temperate zone (40°N – 60°N, 2.20 Tg N yr^{-1}, Figure 1b, e; Table 3). In these regions, average emissions for JJA also noticeably increased from the PI to PD by 2.41 (200%), 0.92 (49%), and 1.09 (98%) TgN yr^{-1}, respectively (Figure 1e; Table 3). The global average emissions for JJA grew by 81% and 4.76 TgN yr^{-1}. The seasonal difference (|DJF-JJA|) in terrestrial N_2O emissions is substantial between 20°S and 60°N with maxima in 20°N to 40°N (Figure 1c, f; Table 3), though the seasonal difference is, on average, close to zero near the equator. Seasonality in emissions also increased from the PI to PD (Figure 1f; Table 3). In addition, the N_2O emissions simulated by the eight TBMs range widely in both seasons and seasonal differences for PD as well as PI period (Figure 1; Table 3) where the large interquartile ranges coincide with high emission regions (Figure S1).

Table 3 Multi-model seasonal N_2O net surface-to-atmosphere fluxes from the land and the ocean for present day (2001-2020) and pre-industrial (1861-1880) periods from different latitudinal zones (TgN yr^{-1}) in DJF (December, January, and February), JJA (June, July, and August), and the absolute differences between these two seasons. Multi-model median and [25^{th} percentile, 75^{th} percentile] of long-term model average are given. Pre-industrial N_2O fluxes from the ocean are only available for Bern3D. N/A: not applicable.

Latitude	Land			Ocean		
	DJF	JJA	|DJF-JJA|	DJF	JJA	|DJF-JJA|
Present day (2001-2020)						
60°N - 90°N	0.02 [0.00, 0.05]	0.35 [0.14, 0.72]	0.32 [0.60, 0.12]	0.01 [-0.03, 0.05]	0.08 [0.05, 0.12]	0.07 [0.15, 0.00]
40°N - 60°N	0.42 [0.22, 0.75]	2.20 [1.24, 3.63]	1.62 [2.99, 0.76]	0.37 [0.18, 0.65]	0.27 [0.21, 0.36]	0.11 [0.12, 0.39]
20°N - 40°N	0.79 [0.46, 1.46]	3.62 [2.43, 5.47]	2.48 [4.20, 1.35]	0.37 [0.10, 0.83]	0.25 [0.19, 0.38]	0.12 [0.16, 0.53]
0° - 20°N	1.36 [0.79, 2.51]	2.78 [1.77, 4.56]	1.18 [2.55, 0.29]	0.81 [0.47, 1.43]	0.79 [0.51, 1.28]	0.01 [0.42, 0.49]
0° - 20°S	2.70 [1.60, 4.47]	1.29 [0.77, 2.52]	1.02 [0.16, 2.38]	0.53 [0.37, 0.97]	0.84 [0.48, 1.76]	0.32 [0.87, 0.05]
20°S - 40°S	0.85 [0.52, 1.46]	0.36 [0.20, 0.62]	0.43 [0.16, 0.91]	0.33 [0.27, 0.47]	0.32 [0.05, 0.81]	0.01 [0.42, 0.30]
40°S - 60°S	0.03 [0.02, 0.05]	0.03 [0.02, 0.04]	0.00 [0.01, 0.01]	0.68 [0.52, 0.83]	0.67 [0.36, 1.04]	0.02 [0.39, 0.32]
60°S - 90°S	NaN	NaN	NaN	0.22 [0.15, 0.32]	0.03 [0.01, 0.09]	0.16 [0.07, 0.27]
Global	6.17 [3.62, 10.75]	10.63 [6.56, 17.58]	4.15 [10.03, 0.78]	3.33 [2.02, 5.55]	3.26 [1.85, 5.83]	0.02 [2.46, 2.24]
Pre-industrial (1861-1880)						
60°N - 90°N	0.01 [0.00, 0.05]	0.28 [0.12, 0.70]	0.26 [0.57, 0.11]	-0.03	0.07	0.10
40°N - 60°N	0.15 [0.06, 0.34]	1.11 [0.59, 1.94]	0.85 [1.59, 0.40]	0.43	0.26	0.17
20°N - 40°N	0.37 [0.18, 0.65]	1.21 [0.74, 2.17]	0.74 [1.62, 0.34]	0.31	0.23	0.08
0° - 20°N	1.08 [0.57, 2.23]	1.86 [1.08, 3.35]	0.56 [1.60, 0.10]	1.07	0.92	0.15
0° - 20°S	2.29 [1.22, 3.95]	1.16 [0.59, 2.35]	0.72 [0.03, 2.00]	1.02	1.93	0.90
20°S - 40°S	0.63 [0.34, 1.13]	0.23 [0.11, 0.46]	0.26 [0.10, 0.69]	0.29	0.43	0.14
40°S - 60°S	0.02 [0.01, 0.03]	0.01 [0.00, 0.02]	0.00 [0.00, 0.01]	0.71	1.07	0.36
60°S - 90°S	NaN	NaN	NaN	0.19	0.07	0.13
Global	4.55 [2.38, 8.38]	5.86 [3.24, 11.00]	1.41 [5.31, 1.95]	4.00	4.96	0.97

The seasonality of land N_2O fluxes was separated by latitudinal regions (Figure 2). The regions with high seasonal differences in N_2O emissions (Table 3), as well as with the highest

annual N_2O emissions (Table 4) in the NH (20°N – 40°N, 0° – 20°N and 40°N – 60°N), show emissions peaking in June to August and a long-term mean seasonal amplitude of 3.84, 1.82, and 2.42 TgN yr^{-1}(multi-model median), respectively, (Figure 2b, c, d; Table 4). The seasonal amplitudes of N_2O emissions from individual land models differ by 2 to 5 folds in these regions. In the SH, the land emissions show the opposite phasing compared to the NH. The N_2O emissions from 0° – 20°S have the strongest seasonality, with a peak in January and an ensemble-median amplitude of 2.04 Tg N yr^{-1}. The model spread is large and seasonal amplitudes differ by more than 7 folds among the land models (Figure 2e). Land N_2O emissions from 60°N – 90°N and 20°S – 40°S are comparably low and show very weak intra-annual variations on absolute terms (Figure 2a, f; Table 4).

Compared to the PI period, the global terrestrial N_2O emissions increased by 36% while the seasonal amplitude by 81% (Table 4). The seasonal amplitude of terrestrial N_2O emissions in the SH increased by 18% for 0° – 20°S and by 107% for 20°S – 40°S. The increase in amplitude is even larger for the NH land, with 35% to 108% for 0° – 20°N, 20°N – 40°N, and 40°N – 60°N (Figure 2; Table 4).

Table 4 Modeled net land and ocean annual N_2O fluxes to the atmosphere from different latitudinal zones (TgN yr^{-1}) and seasonal amplitude (TgN yr^{-1}), quantified by the difference between minimum and maximum flux, for present day (2001-2020) and pre-industrial (1861-1880) periods. Multi-model median and [25th percentile, 75th percentile] of long-term model average are given. Pre-industrial N_2O fluxes from the ocean are only available for Bern3D. N/A: not applicable.

Latitude	Land		Ocean	
	Annual flux	Min-to-max amplitude	Annual flux	Min-to-max amplitude
Present day (2001-2020)				
60°N - 90°N	0.21 [0.05, 0.37]	0.56 [0.22, 0.82]	0.03 [0.01, 0.05]	0.16 [0.12, 0.19]
40°N - 60°N	1.60 [1.38, 1.92]	2.42 [2.27, 3.32]	0.30 [0.24, 0.44]	0.67 [0.37, 0.73]
20°N - 40°N	2.61 [2.45, 2.76]	3.84 [2.80, 4.60]	0.25 [0.18, 0.31]	0.49 [0.30, 0.76]
0° - 20°N	2.77 [2.18, 3.01]	1.82 [1.26, 3.96]	0.94 [0.54, 1.14]	0.77 [0.33, 0.81]
0° - 20°S	2.37 [2.01, 3.04]	2.04 [1.64, 2.46]	1.26 [0.48, 1.43]	1.12 [0.28, 1.13]
20°S - 40°S	0.78 [0.62, 0.90]	0.75 [0.38, 0.92]	0.20 [0.19, 0.24]	0.56 [0.42, 0.58]
40°S - 60°S	0.03 [0.02, 0.04]	0.02 [0.02, 0.03]	0.57 [0.47, 0.66]	0.73 [0.48, 1.04]
60°S - 90°S	N/A	N/A	0.09 [0.07, 0.22]	0.24 [0.18, 0.34]
Global	10.51 [9.80, 11.21]	6.13 [5.17, 7.56]	3.76 [2.91, 4.19]	2.26 [2.11, 2.40]
Pre-industrial (1861-1880)				
60°N - 90°N	0.19 [0.05, 0.42]	0.55 [0.19, 0.79]	0.01	0.13
40°N - 60°N	0.92 [0.67, 1.02]	1.58 [1.27, 1.77]	0.28	0.75
20°N - 40°N	1.02 [0.87, 1.21]	1.85 [0.69, 2.07]	0.20	0.54
0° - 20°N	2.03 [1.89, 2.37]	1.35 [1.05, 2.23]	0.97	0.82
0° - 20°S	2.23 [2.00, 2.50]	1.73 [1.20, 2.72]	1.47	1.21
20°S - 40°S	0.60 [0.48, 0.64]	0.36 [0.30, 0.84]	0.27	0.60
40°S - 60°S	0.02 [0.01, 0.02]	0.01 [0.01, 0.02]	0.71	1.16
60°S - 90°S	N/A	N/A	0.08	0.26
Global	7.73 [6.21, 8.03]	3.39 [2.66, 4.11]	3.99	2.37

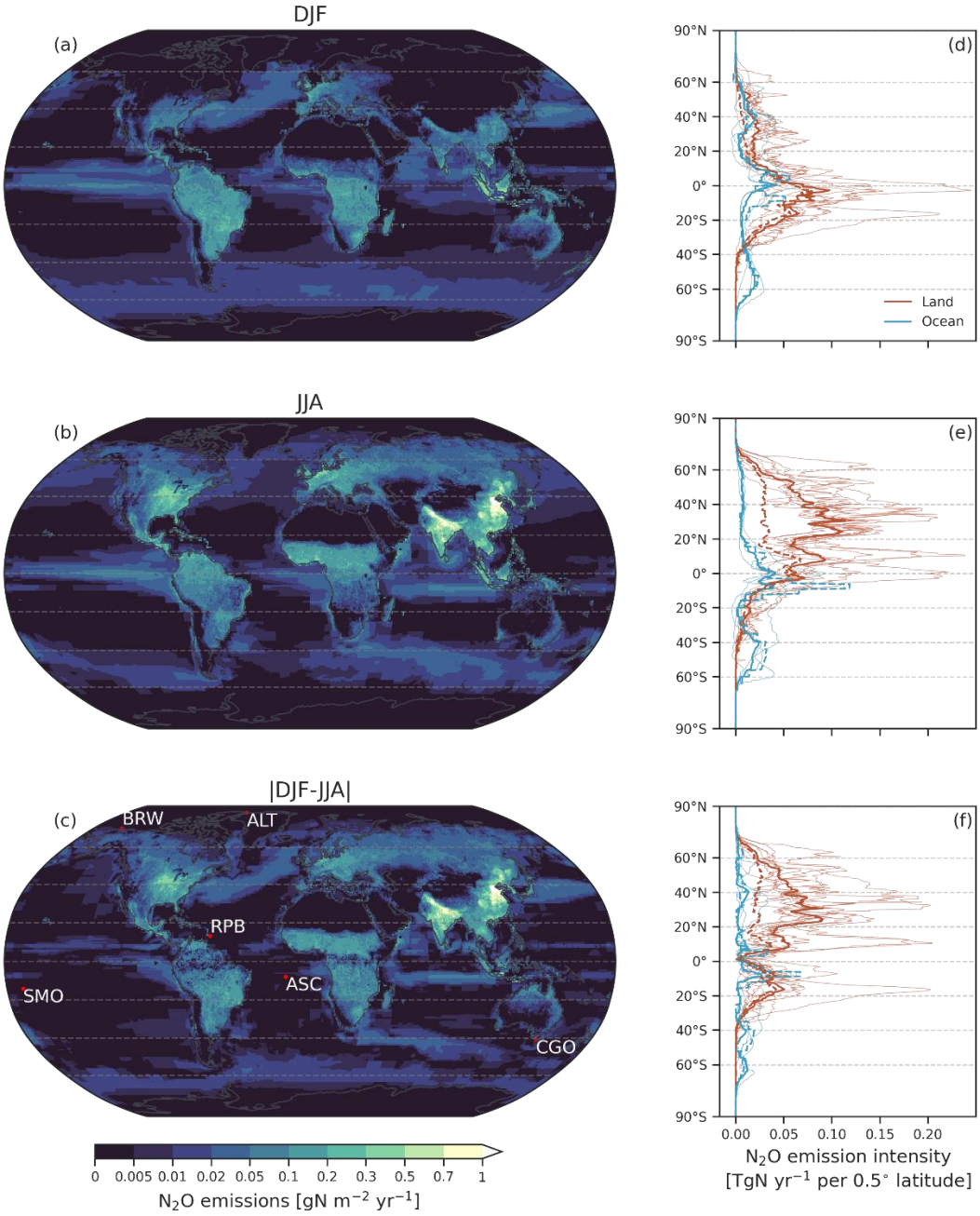

Figure 1 Long-term average N_2O emission density (multi-model median) in recent decades (present day, PD; 2001-2020), from the land and ocean (gN m^{-2} yr^{-1}) for DJF (a, December, January, and February), JJA (b, June, July, and August), and the absolute differences between these two seasons (c), as well as the emissions (TgN yr^{-1}; dark lines: multi-model median; light lines: ensemble members) along the latitudinal gradient resolved by 0.5° for both the land (red lines) and the ocean (blue lines) during PD (solid lines) and pre-industrial period (PI; 1861-1880, dashed lines) (d, e, f). The selected NOAA/CCGG stations are marked by red points in (c) (ALT: Alert, BRW: Barrow, RPB: Ragged Point, ASC: Ascension Island, SMO: Samoa, CGO: Cape Grim). Pre-industrial N_2O fluxes from the ocean are only available for Bern3D.

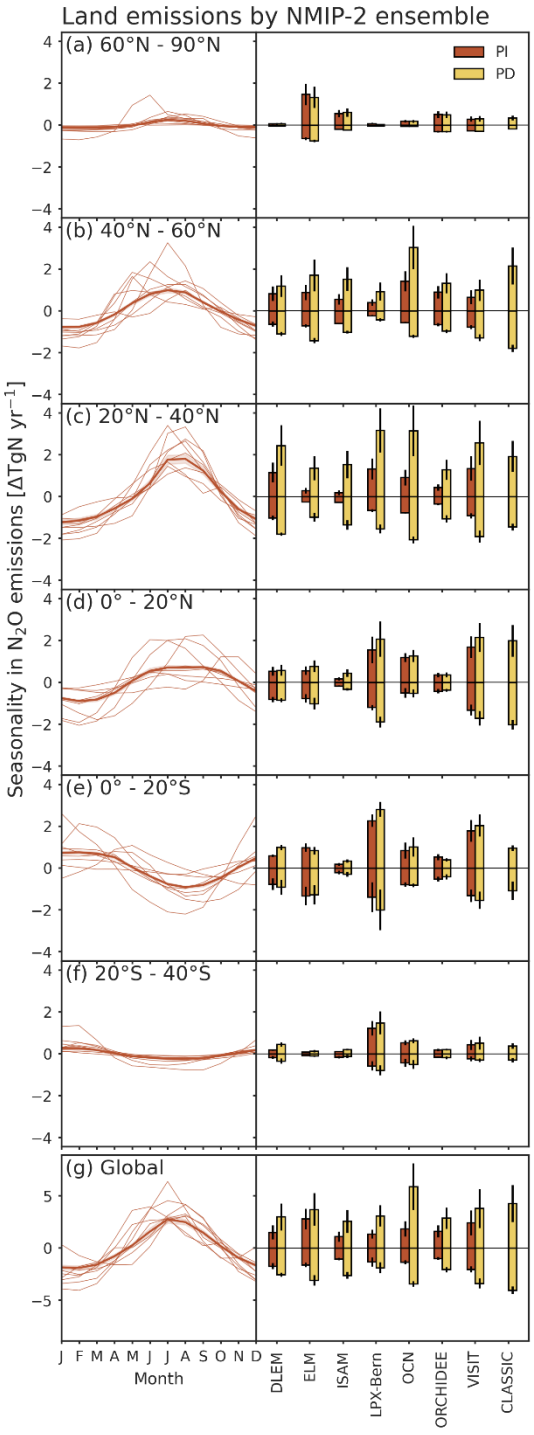

Figure 2 Long-term average seasonality of N_2O emissions for present day (PD, 2001-2020) for different latitudinal zones, and the seasonal minimum and maximum of emissions anomalies for each zone (right panels) during pre-industrial (PI, 1861-1880) and PD periods simulated by NMIP-2 land models respectively. The vertical lines in the right panels indicate ± 1 standard deviation from temporal variability around the period means. Thick lines indicate multi-model median and thin lines individual models in the left panels.

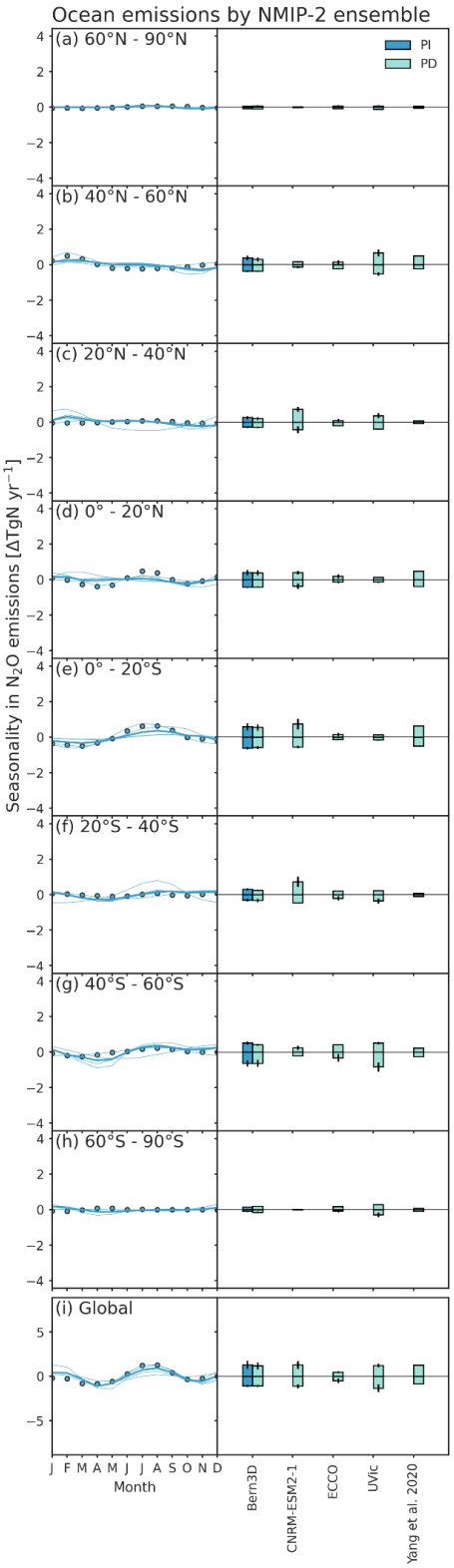

Figure 3 Same as Figure 2 but for the ocean. Circles are reconstructions of a global climatology for monthly ocean N_2O emissions for the period 1988 to 2007 by *Yang et al.* [2020].

3.1.2 Ocean emissions

Monthly ocean N_2O emissions are lower with less intra-annual variation compared to land emissions (Figures 1 and 3; Tables 3 and 4). Seasonal mean ocean emissions during PD show similar patterns during DJF and JJA, with relatively higher emissions from 0° – 20°N, 0° – 20°S, and 40° – 60°S in both seasons (median of 0.53 to 0.84 TgN yr^{-1}). The absolute differences between DJF and JJA are the highest for 0° – 20°S (0.32 TgN yr^{-1}) and 60° – 90°S (0.16 TgN yr^{-1}), while they amount to less than 0.37 TgN yr^{-1} in other regions and globally only 0.02 TgN yr^{-1} (Table 3). Pre-industrial (PI) N_2O fluxes from the ocean are only available for Bern3D, therefore they cannot be compared directly with the multi-model median. The modeled changes in ocean emissions since the PI periods are comparably low in all regions (Figure 1f).

Similar to land emissions, the ocean N_2O emissions also show distinct seasonal cycles with different phasing between the NH and SH for PD (Figure 3). The long-term seasonal amplitudes for most latitudinal zones differ by 3 to 8 folds among the ocean models. However, the seasonal amplitudes of ocean N_2O emissions are usually much smaller than that of land N_2O emissions (ocean: median of up to 1.12 TgN yr^{-1}; land: median of up to 3.84 TgN yr^{-1} for different regions, Table 4), and the seasonality of ocean N_2O emissions remains approximately constant from the PI to PD for Bern3D (Figure 3). A reconstructed global climatology for monthly ocean N_2O emissions from surface N_2O measurements by *Yang et al.* [2020] shows comparable seasonality for all latitudinal zones (blue circles in Figure 3).

Table 5 Selected NOAA/CCGG stations (ALT: Alert, BRW: Barrow, RPB: Ragged Point, ASC: Ascension Island, SMO: Samoa, CGO: Cape Grim) and their seasonal amplitude of atmospheric N_2O mixing ratio (ppb; mean ± 1 standard deviation) observed by flask measurements since 2000 (n = 16 - 19).

ID	Location		Altitude (m a.s.l.)	Min-to-max amplitude		
ALT	82.5°N	62.5°W	210	0.96	±	0.30
BRW	71.3°N	156.6°W	475	1.08	±	0.27
RPB	13.2°N	59.4°W	45	0.53	±	0.18
ASC	7.9°S	14.4°W	54	0.55	±	0.18
SMO	14.3°S	170.6°W	42	1.00	±	0.25
CGO	40.7°S	144.7°E	164	0.83	±	0.31

3.2 Seasonality in observed and modeled atmospheric N_2O

The local aN_2O modeled from land and ocean N_2O fluxes show seasonal cycles, which vary in phase and amplitude for different stations (solid black lines in Figure 4; Table 6). We recall that the net flux from the troposphere-stratosphere exchange is not included in the model, and thus the mismatch between observation and model results largely represents the stratospheric contribution (yellow lines in Figure 4; Table 5 and 6). At the northern high-latitude stations Alert (ALT) and Barrow (BRW), the modeled aN_2O have seasonal cycles with amplitudes of 0.70 and 0.77 ppb (multi-model median) and October maxima during the PD, while the observed seasonal amplitudes are 0.96 ± 0.3 and 1.08 ± 0.27 ppb (long-term mean ± 1 standard deviation),

respectively and have maxima in February-March (grey dots in Figure 4; Table 5). At the tropical station Ragged Point (RPB), the modeled aN_2O seasonal cycle shows similar patterns to the northern high-latitude stations, with October maximum and an amplitude of 0.58 ppb, close to the observed seasonal amplitude of 0.53 ± 0.18 ppb. However, the observed seasonal cycle at these three NH stations is out-of-phase with the modeled cycle with a ca. 5-month delay in maxima. The estimated stratospheric contribution is out-of-phase with respect to the modeled contribution from fluxes and has a larger amplitude at these three NH stations (multi-model median of 1.48, 1.73, and 0.81 for ALT, BRW, and RPB; Table 6). At the SH stations, Ascension Island (ASC) and Samoa (SMO) in the tropics and Cape Grim (CGO) in the mid-latitudes, the modeled aN_2O shows less clear seasonal patterns compared to the NH stations. The modeled seasonal amplitude at ASC is 0.47 ppb with a March maximum and the observed amplitude is 0.55 ± 0.18 ppb with a matching maximum; the modeled amplitude at SMO is 0.39 ppb, much lower than observed (1 ± 0.25 ppb), and the maximum occurs in February in the model and January in the observations; with individual models largely differing in phasing, the modeled amplitude for CGO is the lowest of the six stations at 0.28 ppb, with a February maximum, and also much lower than observed (0.83 ± 0.31), with a December maximum (Figure 4; Table 5 and 6). The stratospheric contributions at these SH stations are estimated to have similar seasonal amplitudes to the observed (multi-model median of 0.63, 0.84, and 0.91 for ASC, SMO, and CGO). The interquartile ranges of the seasonal aN_2O amplitude from uncertainties in surface model fluxes are between 26 to 52% of the median for the six stations.

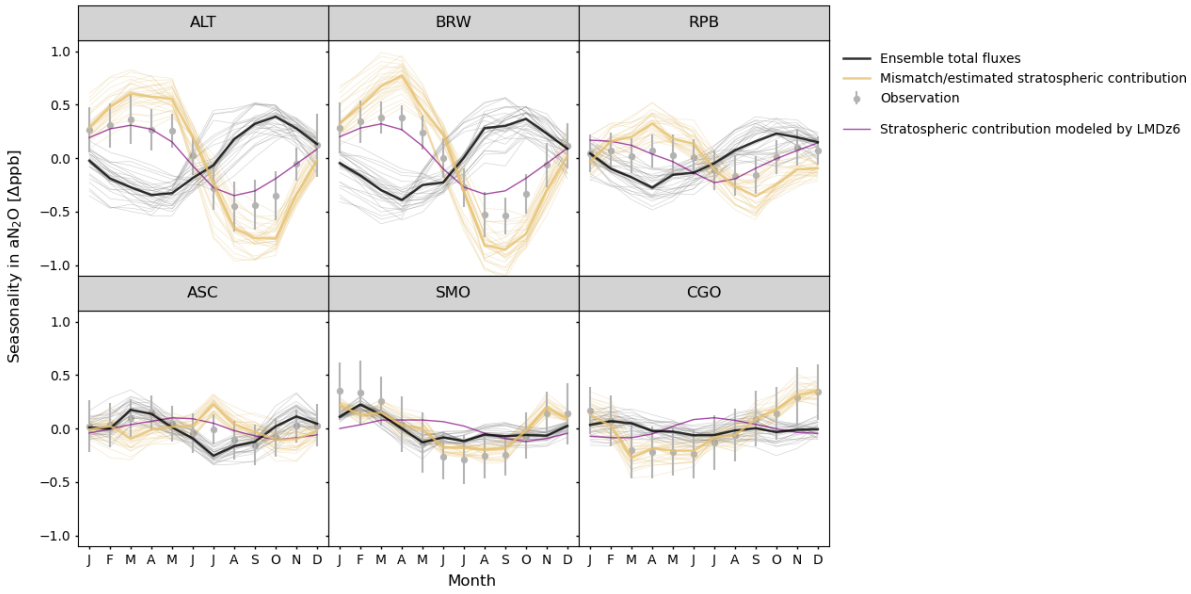

Figure 4 Mismatch (yellow lines) between observed (solid grey circles) and modeled aN_2O seasonality (black lines) at different NOAA/CCGG flask stations (ALT: Alert, BRW: Barrow, CGO: Cape Grim, RPB: Ragged Point, SMO: Samoa, ASC: Ascension Island) for present day (2001-2020). Thick lines indicate multi-model median and thin lines individual model. Vertical lines on grey circles indicate standard deviation from temporal variability weighted by measurement uncertainty. The observation-model mismatch provides an estimate of the stratospheric contribution to aN_2O seasonality from N_2O loss and resulting stratosphere-troposphere net fluxes. A modeled stratospheric tracer of N_2O indicating stratospheric contribution for the same period using the chemistry-transport model, LMDz6 (see *Daniel J. Ruiz and Prather*, [2022] for methods), is shown in purple lines to for comparison.

Table 6 Modeled seasonal min-to-max amplitude of atmospheric N_2O mixing ratio (ppb; multi-model median [25th percentile, 75th percentile] derived from long-term average of modeled aN_2O seasonal cycle) attributed to total of land and ocean emissions as well as separated and the mismatch (estimated stratospheric contribution for present day) at NOAA/CCGG stations (ALT: Alert, BRW: Barrow, RPB: Ragged Point, ASC: Ascension Island, SMO: Samoa, CGO: Cape Grim). Pre-industrial N_2O fluxes from the ocean are only available for Bern3D.

Site	Present day (2001-2020)				Pre-industrial (1861-1880)		
	Land + ocean	Land	Ocean	Mismatch	Land + ocean	Land	Ocean
ALT	0.70 [0.65, 0.85]	0.78 [0.71, 0.94]	0.16 [0.15, 0.18]	1.48 [1.39, 1.60]	0.44 [0.38, 0.50]	0.48 [0.39, 0.56]	0.14
BRW	0.77 [0.67, 0.87]	0.80 [0.72, 0.93]	0.19 [0.18, 0.22]	1.73 [1.64, 1.89]	0.43 [0.36, 0.50]	0.49 [0.41, 0.57]	0.17
RPB	0.58 [0.45, 0.69]	0.60 [0.51, 0.70]	0.18 [0.15, 0.20]	0.81 [0.65, 0.98]	0.54 [0.41, 0.56]	0.47 [0.36, 0.48]	0.20
ASC	0.47 [0.42, 0.59]	0.41 [0.37, 0.46]	0.18 [0.14, 0.22]	0.63 [0.60, 0.68]	0.48 [0.40, 0.49]	0.30 [0.28, 0.37]	0.26
SMO	0.39 [0.36, 0.46]	0.32 [0.27, 0.39]	0.14 [0.12, 0.17]	0.84 [0.82, 0.90]	0.29 [0.21, 0.32]	0.22 [0.14, 0.27]	0.14
CGO	0.28 [0.23, 0.38]	0.25 [0.21, 0.34]	0.25 [0.24, 0.29]	0.91 [0.85, 0.96]	0.24 [0.20, 0.26]	0.19 [0.14, 0.26]	0.24

3.2.1 Contributions from land versus ocean N_2O emissions

When transporting N_2O emissions from the land (solid red lines in Figure 5) and the ocean (solid blue lines in Figure 5) separately, the corresponding aN_2O seasonal cycles differ by phasing and amplitude at all stations (Figure 5; Table 6). The seasonal aN_2O amplitude resulting from land N_2O emissions (0.32 to 0.80 ppb, multi-model median) is generally larger than from ocean N_2O emissions (0.14 to 0.29 ppb), except for CGO (0.25 ppb from both land and ocean; Table 6). Moreover, due to the differences in seasonal aN_2O phasing from land versus ocean fluxes, the modeled aN_2O seasonal amplitudes from only land emissions are slightly larger than those from total emissions at NH stations (by 0.01 to 0.08 ppb), and smaller at SH stations (by 0.02 to 0.07 ppb; Table 6). Furthermore, the modeled aN_2O seasonality from total N_2O emissions has a similar phasing compared to that from only land emissions at all stations, except for CGO, where ocean emissions strongly influence aN_2O seasonality. (Figure 5; Table 6). The interquartile ranges of the seasonal aN_2O amplitude are between 21 to 52% of the median from uncertainties in land model fluxes and between 17 to 42% from uncertainties in ocean model fluxes for the six stations.

For the pre-industrial (PI) period, modeled aN_2O seasonal cycles have a similar phasing to that of PD (dashed lines for PI and solid lines for PD in Figure 5). The PI ocean N_2O emissions are only available by Bern3D, showing small PD-PI differences (Figure 5). The seasonal amplitudes attributed to land N_2O fluxes increase at least by 26 % at all stations (PI: 0.19 to 0.49 ppb; PD: 0.25 to 0.80 ppb, Table 6), with the largest PD-PI differences at the northern high-latitude stations (ALT and BRW), by 0.29 and 0.31 ppb (61 and 64 %, Table 6).

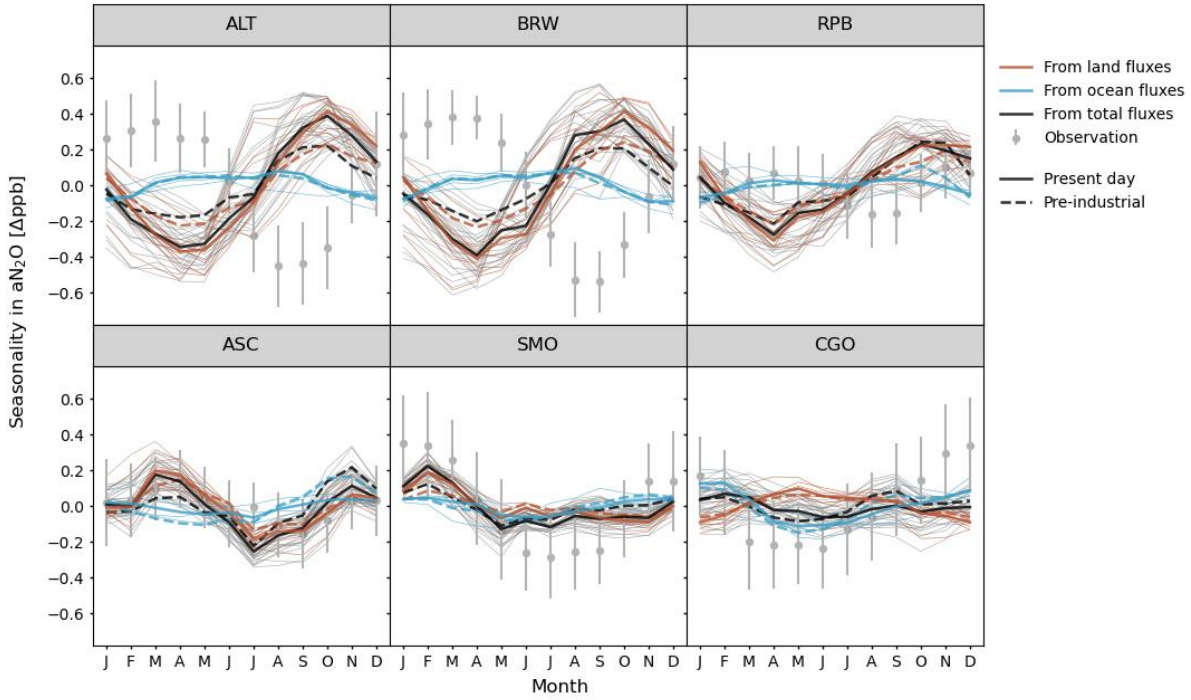

Figure 5 Long-term average seasonality of observed aN_2O (solid grey circles) and modeled aN_2O (lines) at different NOAA/CCGG flask stations (ALT: Alert, BRW: Barrow, RPB: Ragged Point, ASC: Ascension Island, SMO: Samoa, CGO: Cape Grim). Modeled aN_2O seasonality are attributed to the N_2O emissions from the land (solid red lines) and the ocean (solid blue lines), and total emissions (solid black lines) for present day (2001-2020). Only the multi-model median of aN_2O seasonality for the pre-industrial period (1861-1880) is given (dashed lines). Thick lines indicate multi-model median and thin lines individual models. Vertical lines on grey circles indicate observed temporal variability weighted with measurement uncertainty.

3.2.2 Influence of intra-annual variation versus spatial pattern of N_2O emissions

Next, we quantify the contributions to aN_2O seasonality resulting from the intra-annual variations in flux versus those from the deseasonalized spatial flux pattern. The deseasonalized spatial pattern can cause seasonal variations in aN_2O due to seasonally varying atmospheric transport. The intra-annual variation is obtained by using the detrended N_2O fluxes as sources for the atmospheric transport model, while the remaining influence is obtained by the running mean of N_2O fluxes (ALT, SMO in Figure 6; BRW, RPB, ASC, CGO in Figure S2). Besides, industrial emissions that do not vary by season could also contribute to the spatial pattern but are not considered in this study.

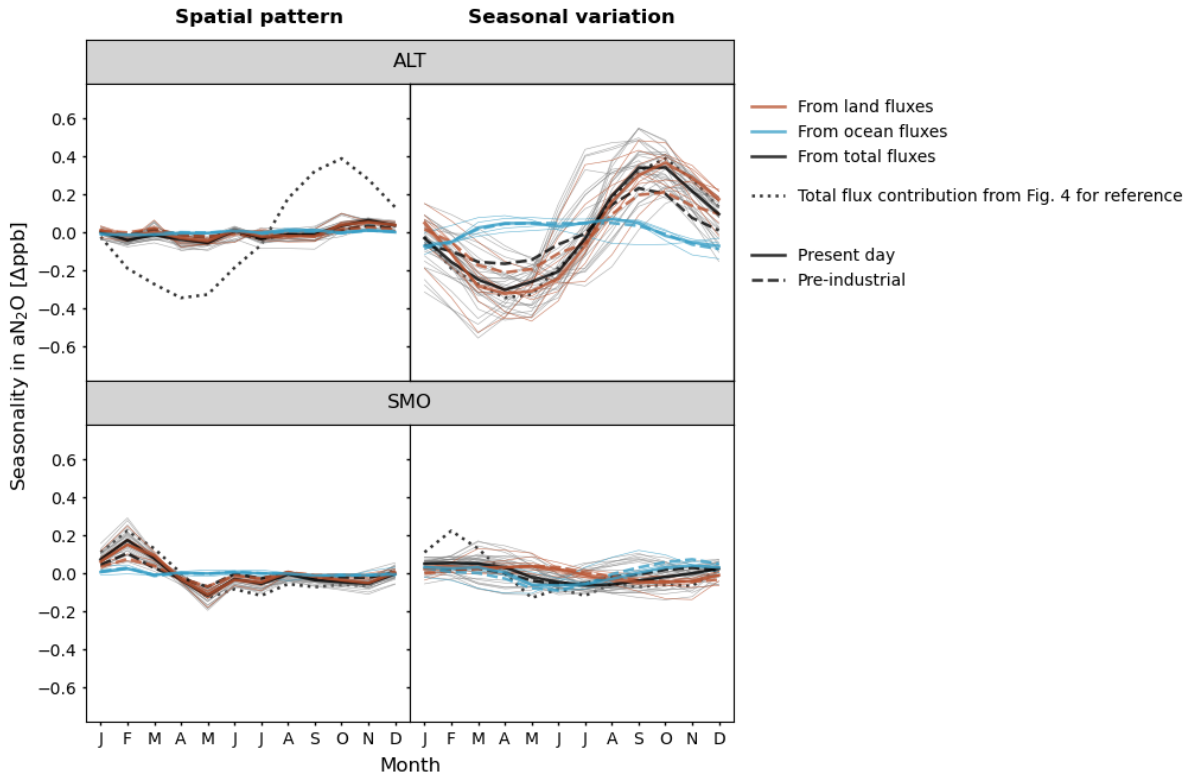

Figure 6 Modeled aN_2O seasonality at different NOAA/CCGG flask stations (ALT: Alert; SMO: Samoa) from spatial pattern (deseasonalized fluxes as 12-month running mean) and seasonal variation (detrended fluxes) of N_2O fluxes for pre-industrial period (1861-1880; dashed lines) and present day (2001-2020; solid lines). Only the multi-model median of aN_2O seasonality for the pre-industrial period (1861-1880) is given (dashed lines). Thick lines indicate multi-model median and thin lines individual models. The aN_2O seasonality modeled from total (including both spatial and seasonal variations) land and ocean N_2O emissions of present day are repeated for reference in all panels.

At the NH stations (ALT, BRW, and RPB), the (detrended) seasonal cycle of N_2O emissions leads to similar phasing and amplitude for aN_2O seasonality (multi-model median: 0.66, 0.71, and 0.46 ppb, respectively) as when using total emissions (Figure 6 and S2; Table S1). The seasonal amplitude of aN_2O from 12-month running mean fluxes is small (0.17 to 0.21 ppb, Table S1), suggesting both land and ocean N_2O emissions contribute to the seasonality of aN_2O mainly via their seasonal cycles at the NH stations. At the tropical stations in the SH (ASC and SMO), both phasing and amplitude of aN_2O seasonality are affected slightly more by the spatial pattern (amplitude of 0.35 and 0.28 ppb) than the seasonality of N_2O fluxes (0.28 and 0.23 ppb, Figure 6 and S2; Table S1). For the SH mid-latitude station CGO, land N_2O fluxes have similar impacts on the aN_2O seasonal amplitude via their spatial pattern (0.19 ppb) than their seasonality (0.21 ppb), while ocean fluxes have a stronger impact via their seasonality (0.22 ppb) than their spatial pattern (0.06 ppb). The combined fluxes shows a larger impact via their seasonality (0.28 ppb) than their spatial pattern (0.14 ppb). In summary, the impacts of temporal variation and spatial patterns of N_2O fluxes differ largely by site.

4 Discussion

Our results show large spatial and temporal variations and a pronounced seasonality in N_2O surface-to-atmosphere fluxes. The variations and seasonality of N_2O emissions from the land biosphere are stronger than those from the ocean. The largest increase in the seasonal amplitude of emissions over the industrial period (1861-1880 to 2001-2020) is found over land between 20°N and 40°N, with an industrial period increase in the seasonal amplitude of 108% (multi-model median; Table 4). The increasing seasonality of land emissions is attributed, using the factorial simulations of the NMIP project [*Tian et al.*, 2018], to anthropogenic causes. The responsible activities mainly are fertilizer applications in arable lands [see *Cardenas et al.*, 2013; *Fuchs et al.*, 2020; *Tian et al.*, 2019] and land-use change such as converting natural land cover to intensively managed croplands or pasture [*Petitjean et al.*, 2015]. Besides, considerable model spread in seasonal emissions (Figures 1 and S1) and min-to-max amplitude (Figures 2 and 3) of N_2O emissions are noted for all latitudinal zones.

Modern land and ocean N_2O fluxes contribute to tropospheric N_2O (aN_2O) seasonality to different extents at different stations (Figure 5; Table 6). The influence of these fluxes on aN_2O always results in combination with seasonally and spatially varying atmospheric transport. For all stations except CGO, land N_2O emissions influence aN_2O seasonality more than ocean N_2O emissions, predominantly via their seasonal cycles at NH stations (ALT, Figure 6; BRW and RBP, Figure S2; Table S1) while mainly via deseasonalized spatial patterns at remote tropical stations in the SH (SMO, Figure 6; ASC, Figure S2; Table S1). At CGO, ocean N_2O fluxes show a slightly stronger impact on aN_2O seasonality via their seasonal cycles (Figure S2, Table S1). These results suggest that total fluxes as opposed to detrended fluxes should be used to quantify the overall influence of N_2O emissions on aN_2O seasonality.

Generally, the measured aN_2O seasonality is considered to be an outcome of seasonal surface emissions, tropospheric transport, stratospheric loss, and stratosphere-to-troposphere exchange (STE) [e.g., *Bouwman and Taylor*, 1996; *Nevison et al.*, 2005; *D. J. Ruiz et al.*, 2021]. Our simulated aN_2O seasonality using TM2 represents only the contribution from surface fluxes and predominantly tropospheric transport, whereas stratospheric N_2O loss and resulting net fluxes by STE are not included. Thus, the mismatch between our modeled and the observed aN_2O seasonality (Figure 4, yellow lines) can be understood to represent the stratospheric contribution to the aN_2O seasonal cycle, with some uncertainty due to the uncertainty in modeling surface N_2O emissions and atmospheric transport (see also Fig 5 of *D. J. Ruiz et al.*, [2021] and Fig 5 of *Daniel J. Ruiz and Prather*, [2022]). At the northern hemisphere (NH) sites (ALT, BRW, and RPB), the estimated stratospheric contributions to aN_2O (Figure 4), have a minimum in August-September, nearly 6 months out-of-phase with the contributions from surface fluxes. The stratospheric contributions have large amplitudes and apparently dominate the observed seasonality at these NH sites, particularly at the high-altitude sites ALT and BRW. The phasing of our estimated stratospheric contributions is consistent with a stratospheric tracer of N_2O modeled using the chemistry-transport model, LMDz6 (following the method outlined in [*Daniel J. Ruiz and Prather*, 2022], purple lines in Figure 4) with a maximum influence of STE in August and September in the northern extratropic. At the tropical sites (ASC and SMO) there is less influence from STE, and thus the observed seasonality of aN_2O is likely mostly driven by land emissions and tropospheric transport. At the southern hemisphere (SH) mid-latitude site, CGO, our estimated stratospheric contribution has a minimum in March (Figure 4) and is thus 6 months out-of-phase with the NH, as expected. Furthermore, the amplitude of the estimated

stratospheric contribution is much smaller than in the NH (Table 6), which again is as expected owing to the smaller seasonal amplitude of the STE net fluxes in the SH [*James et al.*, 2003; *Daniel J. Ruiz and Prather*, 2022] and at the sites (Figure 4, purple lines). Moreover, at CGO, the surface flux influence is only 3 months out-of-phase with that of the estimated stratospheric contribution, and the combination of both leads to the observed minimum in May-June. *Nevison et al.* [2005] by analyzing the source contributions to aN_2O seasonality at Cape Grim show the stratospheric influence with similar phasing (April minimum) to our estimated stratospheric influence at Cape Grim.

We demonstrate that surface N_2O emissions contribute substantially to aN_2O seasonality, although the phase of the observed seasonal cycle in the NH mid to high latitudes is out-of-phase with the influence of surface fluxes and tropospheric transport. The impact of land N_2O emissions on aN_2O seasonality is modeled to have increased considerably (61, 64, and 26 % at ALT, BRW, and RPB, respectively) over the industrial period (Figure 5; Table 6). *Ruiz et al.* [2021] suggest that the observed seasonality of aN_2O in the NH is explained by net fluxes from STE rather than surface emissions. However, we show that the influence of surface emissions is an important contribution to the net seasonal cycle, and without it, the seasonal amplitude would be larger by 39 to 126% in the NH mid to high latitudes with a later minimum by ~1 month (Figure 4). With global change and likely increasing N-fertilizer use, terrestrial biosphere N_2O emissions are potentially continuing to increase in the future thus leading to a more important contribution of these emissions to the seasonal cycle of aN_2O in the years to come. This future increase in the contribution from land N_2O fluxes is possibly lowering the seasonal amplitude and causing a shift in phasing for aN_2O seasonality, especially in high-latitude regions.

Furthermore, the atmospheric transport matrix of TM2 [*Kaminski et al.*, 1999] used in this work represents a single-year meteorological field and hence cannot account for atmospheric cycles and climate patterns with a non-annual frequency, such as Quasi-Biennial Oscillation and El Nino/La Nina Southern Oscillation which have substantial impacts especially for low latitude regions, namely ASC and SMO in this study. Moreover, *Thompson et al.* [2014] compared a set of chemistry-transport models that consider different annual meteorological fields and showed considerable model spread in both phasing and amplitude for modeled aN_2O seasonality. Thus, uncertainties from transport models also impose additional challenges in assessing source contributions to aN_2O variations and in comparing results across studies.

There is a large model spread in N_2O emissions (Figure 1d-f, Figure S1) as well as their seasonal amplitudes (the interquartile range is 28 to 148 % of the multi-model median of land and ocean seasonal amplitude for different latitudinal zones, Figure 2; Table 4). For land emissions which is the main source of N_2O, important processes of the coupled nitrogen-carbon-water cycles are represented differently among NMIP models (see evaluation of some of the models by *Kou-Giesbrecht et al.*, 2023]), contributing to the large model spread in emissions. Further, there are uncertainties in N fertilizer application schemes, for instance, the application timing for synthetic fertilizers as well as the usage of manure fertilizers. The spread in emissions translates to a considerable range in modeled aN_2O seasonal cycle (interquartile range is 21 to 52% of the multi-model median for the land contribution to the aN_2O seasonal amplitude, and 17 to 42% for the ocean contribution across sites, Figure 5; Table 6).

Our study suggests that drivers for the seasonality of aN_2O vary by site and land N_2O emissions have become increasingly influential. Our understanding of the N cycle would benefit greatly from further efforts to reduce uncertainties lying in processes from surface fluxes to

atmospheric transport and chemistry. Future research considering observations and models can provide further evidence for the sources and impacts of N_2O emissions.

5 Conclusions and outlook

Our results demonstrate that surface N_2O fluxes contribute significantly to the seasonality of tropospheric N_2O at different observation sites. The model results from the Nitrogen/N_2O Model Intercomparison Project suggest a strong increase in the seasonal variation of terrestrial biosphere N_2O emissions over the industrial period with an amplifying influence on the seasonality of tropospheric N_2O. The wide range of spatial and temporal variations simulated among NMIP-2 models calls for model improvements and validations on different scales. In situ aN_2O observations, in combination with atmospheric chemistry and transport models, may provide a potential novel top-down constraint for nitrogen-N_2O-enabled land biosphere modeling.

Acknowledgements

The authors thank Thomas Kaminski for providing the atmospheric transport matrix. This study was supported by the Swiss National Science Foundation (200020 200511). AI was supported by the Environmental Research and Technology Development Fund (JPMEERF21S20830) of the Ministry of the Environment and the Environmental Restoration and Conservation Agency of Japan. QZ acknowledges the support from the U.S. Department of Energy through the Reducing Uncertainties in Biogeochemical Interactions through Synthesis and Computation Scientific Focus Area (RUBISCO SFA) project. HT and NP acknowledge the funding support from the U.S. National Science Foundation (Grant number: 1903722). RLT acknowledges funding through the Copernicus Atmosphere Monitoring Service (https://atmosphere.copernicus. eu/), implemented by ECMWF on behalf of the European Commission and computing resources provided by LSCE.

Open Research

The NMIP-2 model outputs are available on request to Hanqin Tian (hanqin.tian@bc.edu). The ocean model outputs are available on request to Parvadha Suntharalingam (P.Suntharalingam@uea.ac.uk) or Pierre Regnier (pierre.regnier@ulb.be). aN_2O observation data are available on the website of NOAA/CCGG (https://gml.noaa.gov/ccgg/trends_n2o/). Other datasets used in this study are available upon contacting the correspondence author.

The scripts for reproducing the figures will be available on Zenodo.

References

Bakker, D. C. E., et al. (2014), Air-sea interactions of natural long-lived greenhouse gases (CO2, N2O, CH4) in a changing climate, in *Ocean-Atmosphere Interactions of Gases and Particles*, edited, pp. 113-169.

Battaglia, G., and F. Joos (2018), Marine N2O Emissions From Nitrification and Denitrification Constrained by Modern Observations and Projected in Multimillennial Global Warming Simulations, *Global Biogeochemical Cycles, 32*(1), 92-121.

564 Bergamaschi, P., et al. (2015), Top-down estimates of European CH4 and N2O emissions based
565 on four different inverse models, *Atmospheric Chemistry and Physics*, *15*(2), 715-736.
566 Bouwman, A. F., and J. A. Taylor (1996), Testing high-resolution nitrous oxide emission
567 estimates against observations using an atmospheric transport model, *Global*
568 *Biogeochemical Cycles*, *10*(2), 307-318.
569 Breider, F., C. Yoshikawa, A. Makabe, S. Toyoda, M. Wakita, Y. Matsui, S. Kawagucci, T.
570 Fujiki, N. Harada, and N. Yoshida (2019), Response of N2O production rate to ocean
571 acidification in the western North Pacific, *Nature Climate Change*, *9*(12), 954-+.
572 Butterbach-Bahl, K., E. M. Baggs, M. Dannenmann, R. Kiese, and S. Zechmeister-Boltenstern
573 (2013), Nitrous oxide emissions from soils: how well do we understand the processes and
574 their controls?, *Philos T R Soc B*, *368*(1621).
575 Canadell, J. G., et al. (2021), Global Carbon and other Biogeochemical Cycles and Feedbacks. In
576 Climate Change 2021: The Physical Science Basis. Contribution of Working Group I to the
577 Sixth Assessment Report of the Intergovernmental Panel on Climate Change*Rep.*, V.
578 Masson-Delmotte, P. Zhai, A. Pirani, S.L. Connors, C. Péan, S. Berger, N. Caud, Y. Chen,
579 L. Goldfarb, M.I. Gomis, M. Huang, K. Leitzell, E. Lonnoy, J.B.R. Matthews, T.K.
580 Maycock, T. Waterfield, O. Yelekçi, R. Yu, and B. Zhou (eds.) (eds.), 673–816 pp, IPCC,
581 Cambridge, United Kingdom and New York, NY, USA, doi: 10.1017/9781009157896.007.
582 Cardenas, L. M., et al. (2013), Towards an improved inventory of N2O from agriculture: Model
583 evaluation of N2O emission factors and N fraction leached from different sources in UK
584 agriculture, *Atmos Environ*, *79*, 340-348.
585 Crutzen, P. J. (1970), Influence of Nitrogen Oxides on Atmospheric Ozone Content, *Q J Roy*
586 *Meteor Soc*, *96*(408), 320-325.
587 Dijkstra, F. A., S. A. Prior, G. B. Runion, H. A. Torbert, H. Tian, C. Lu, and R. T. Venterea
588 (2012), Effects of elevated carbon dioxide and increased temperature on methane and
589 nitrous oxide fluxes: evidence from field experiments, *Frontiers in Ecology and the*
590 *Environment*, *10*(10), 520-527.
591 Dlugokencky, E., et al. (2021), Measurements of CO2, CH4, CO, N2O, H2, SF6 and isotopic
592 ratios in flask-air samples at global and regional background sites starting in 1967, edited
593 by G. M. L. NOAA Earth System Research Laboratories.
594 Fischer, H., et al. (2018), Palaeoclimate constraints on the impact of 2 degrees C anthropogenic
595 warming and beyond, *Nature Geoscience*, *11*(7), 474-485.
596 Fischer, H., et al. (2019), N2O changes from the Last Glacial Maximum to the preindustrial -
597 Part 1: Quantitative reconstruction of terrestrial and marine emissions using N2O stable
598 isotopes in ice cores, *Biogeosciences*, *16*(20), 3997-4021.
599 Forster, P., T. Storelvmo, K. Armour, W. Collins, J.-L. Dufresne, D. Frame, D. Lunt, T.
600 Mauritsen, M. Palmer, and M. Watanabe (2021), The Earth's energy budget, climate
601 feedbacks, and climate sensitivity*Rep.*, V. Masson-Delmotte, et al. (eds.), Cambridge
602 University Press, London, UK.
603 Fuchs, K., et al. (2020), Evaluating the Potential of Legumes to Mitigate N2O Emissions From
604 Permanent Grassland Using Process-Based Models, *Global Biogeochemical Cycles*,
605 *34*(12).
606 Ganesan, A. L., et al. (2020), Marine Nitrous Oxide Emissions From Three Eastern Boundary
607 Upwelling Systems Inferred From Atmospheric Observations, *Geophysical Research*
608 *Letters*, *47*(14), e2020GL087822.

Harris, I. C. (2021), CRU JRA v2.2: A forcings dataset of gridded land surface blend of Climatic Research Unit (CRU) and Japanese reanalysis (JRA) data; Jan.1901 - Dec.2020, edited by N. E. C. f. E. D. Analysis, University of East Anglia Climatic Research Unit.

Hegglin, M., D. Kinnison, and J.-F. Lamarque (2016), CCMI nitrogen surface fluxes in support of CMIP6 - version 2.0, edited, Earth System Grid Federation.

Heimann, M. (1995), The global atmospheric tracer model TM2*Rep.* (eds.), Germany.

Hirsch, A. I., A. M. Michalak, L. M. Bruhwiler, W. Peters, E. J. Dlugokencky, and P. P. Tans (2006), Inverse modeling estimates of the global nitrous oxide surface flux from 1998-2001, *Global Biogeochemical Cycles*, *20*(1), n/a-n/a.

Hoyer, S., and J. Hamman (2017), xarray: labeled arrays and datasets in Python, in *Journal of Open Research Software*, edited, Ubiquity Press.

Hunter, J. D. (2007), Matplotlib: A 2D graphics environment, *Computing in Science & Engineering*, *9*(3), 90-95.

Hurtt, G. C., et al. (2020), Harmonization of global land use change and management for the period 850-2100 (LUH2) for CMIP6, *Geosci Model Dev*, *13*(11), 5425-5464.

Hutchins, D. A., and D. C. Capone (2022), The marine nitrogen cycle: new developments and global change, *Nat Rev Microbiol*, *20*(7), 401-414.

IPCC (2021), Climate Change 2021: The Physical Science Basis. Contribution of Working Group I to the Sixth Assessment Report of the Intergovernmental Panel on Climate Change*Rep.*, V. Masson-Delmotte, et al. (eds.), Cambridge University Press, Cambridge, United Kingdom and New York, NY, USA, doi: 10.1017/9781009157896.

IPCC (2022), Climate Change 2022: Impacts, Adaptation, and Vulnerability*Rep.*, H.-O. Pörtner, et al. (eds.), Cambridge University Press. In Press.

Ito, A., K. Nishina, K. Ishijima, S. Hashimoto, and M. Inatomi (2018), Emissions of nitrous oxide (N_2O) from soil surfaces and their historical changes in East Asia: a model-based assessment, Progress in Earth and Planetary Science, 5(55), 10.1186/s40645-40018-40215-40644. 10.1186/s40645-018-0215-4

James, P., A. Stohl, C. Forster, S. Eckhardt, P. Seibert, and A. Frank (2003), A 15-year climatology of stratosphere-troposphere exchange with a Lagrangian particle dispersion model - 2. Mean climate and seasonal variability, *J Geophys Res-Atmos*, *108*(D12).

Jiang, X., W. L. Ku, R.-L. Shia, Q. Li, J. W. Elkins, R. G. Prinn, and Y. L. Yung (2007), Seasonal cycle of N_2O: Analysis of data, *Global Biogeochemical Cycles*, *21*(1).

Joos, F., and R. Spahni (2008), Rates of change in natural and anthropogenic radiative forcing over the past 20,000 years, *P Natl Acad Sci USA*, *105*(5), 1425-1430.

Joos, F., R. Spahni, B. D. Stocker, S. Lienert, J. Muller, H. Fischer, J. Schmitt, I. C. Prentice, B. Otto-Bliesner, and Z. Y. Liu (2020), N2O changes from the Last Glacial Maximum to the preindustrial - Part 2: terrestrial N2O emissions and carbon-nitrogen cycle interactions, *Biogeosciences*, *17*(13), 3511-3543.

Kaminski, T., M. Heimann, and R. Giering (1999), A coarse grid three-dimensional global inverse model of the atmospheric transport - 1. Adjoint model and Jacobian matrix, *J Geophys Res-Atmos*, *104*(D15), 18535-18553.

Kock, A., and H. W. Bange (2015), Counting the ocean's greenhouse gas emissions, *Eos (Washington. DC)*, *96*(3), 10–13.

Kou-Giesbrecht, S., et al. (2023), Evaluating nitrogen cycling in terrestrial biosphere models: a disconnect between the carbon and nitrogen cycles, *Earth Syst. Dynam.*, *14*(4), 767-795.

Landolfi, A., C. J. Somes, W. Koeve, L. M. Zamora, and A. Oschlies (2017), Oceanic nitrogen cycling and N2O flux perturbations in the Anthropocene, *Global Biogeochemical Cycles*, *31*(8), 1236-1255.

Lan, X., K.W. Thoning, and E. J. Dlugokencky (2023a), Trends in globally-averaged CH4, N2O, and SF6 determined from NOAA Global Monitoring Laboratory measurements. Version 2023-03, url: https://doi.org/10.15138/P8XG-AA10, last access date: 08 March 2023.

Lan, X., P. Tans, and K.W. Thoning (2023b), Trends in globally-averaged CO2 determined from NOAA Global Monitoring Laboratory measurements. Version 2023-03 NOAA/GML, url: gml.noaa.gov/ccgg/trends/, last access date: 08 March 2023.

Liang, Q., A. R. Douglass, B. N. Duncan, R. S. Stolarski, and J. C. Witte (2009), The governing processes and timescales of stratosphere-to-troposphere transport and its contribution to ozone in the Arctic troposphere, *Atmospheric Chemistry and Physics*, *9*(9), 3011-3025.

Liang, Q., C. Nevison, E. Dlugokencky, B. D. Hall, and G. Dutton (2022), 3-D Atmospheric Modeling of the Global Budget of N_2O and its Isotopologues for 1980–2019: The Impact of Anthropogenic Emissions, *Global Biogeochemical Cycles*, *36*(7).

Ma, M. N., C. Q. Song, H. J. Fang, J. B. Zhang, J. Wei, S. R. Liu, X. Z. Chen, K. R. Zhang, W. P. Yuan, and H. B. Lu (2022), Development of a Process-Based N2O Emission Model for Natural Forest and Grassland Ecosystems, *J Adv Model Earth Sy*, *14*(3).

MacFarling Meure, C., D. Etheridge, C. Trudinger, P. Steele, R. Langenfelds, T. van Ommen, A. Smith, and J. Elkins (2006), Law Dome CO2, CH4 and N2O ice core records extended to 2000 years BP, *Geophysical Research Letters*, *33*(14).

Manizza, M., R. F. Keeling, and C. D. Nevison (2012), On the processes controlling the seasonal cycles of the air-sea fluxes of O-2 and N2O: A modelling study, *Tellus B*, *64*.

Martins, M. D., et al. (2022), Modeling N2O emissions of complex cropland management in Western Europe using DayCent: Performance and scope for improvement, *Eur J Agron*, *141*.

Mueller, R. (2021), The impact of the rise in atmospheric nitrous oxide on stratospheric ozone This article belongs to Ambio's 50th Anniversary Collection. Theme: Ozone Layer, *Ambio*, *50*(1), 35-39.

Nevison, C. D., R. F. Keeling, R. F. Weiss, B. N. Popp, X. Jin, P. J. Fraser, L. W. Porter, and P. G. Hess (2005), Southern Ocean ventilation inferred from seasonal cycles of atmospheric N2O and O2/N2 at Cape Grim, Tasmania, *Tellus B: Chemical and Physical Meteorology*, *57*(3), 218-229.

Nevison, C. D., et al. (2011), Exploring causes of interannual variability in the seasonal cycles of tropospheric nitrous oxide, *Atmospheric Chemistry and Physics*, *11*(8), 3713-3730.

Pastorello, G., et al. (2020), The FLUXNET2015 dataset and the ONEFlux processing pipeline for eddy covariance data, *Scientific Data*, *7*(1), 225.

Patra, P. K., et al. (2022), Forward and Inverse Modeling of Atmospheric Nitrous Oxide Using MIROC4-Atmospheric Chemistry-Transport Model, *Journal of the Meteorological Society of Japan. Ser. II*, *100*(2), 361-386.

Petitjean, C., C. Henault, A. S. Perrin, C. Pontet, A. Metay, M. Bernoux, T. Jehanno, A. Viard, and J. C. Roggy (2015), Soil N2O emissions in French Guiana after the conversion of tropical forest to agriculture with the chop-and-mulch method, *Agr Ecosyst Environ*, *208*, 64-74.

Prather, M. J., et al. (2015), Measuring and modeling the lifetime of nitrous oxide including its variability, *Journal of Geophysical Research: Atmospheres*, *120*(11), 5693-5705.

Ravishankara, A. R., J. S. Daniel, and R. W. Portmann (2009), Nitrous Oxide (N_2O): The Dominant Ozone-Depleting Substance Emitted in the 21st Century, *Science*, *326*(5949), 123-125.

Rubino, M., et al. (2019), Revised records of atmospheric trace gases CO2, CH4, N2O, and delta C-13-CO2 over the last 2000 years from Law Dome, Antarctica, *Earth System Science Data*, *11*(2), 473-492.

Ruiz, D. J., and M. J. Prather (2022), From the middle stratosphere to the surface, using nitrous oxide to constrain the stratosphere–troposphere exchange of ozone, *Atmospheric Chemistry and Physics*, *22*(3), 2079-2093.

Ruiz, D. J., M. J. Prather, S. E. Strahan, R. L. Thompson, L. Froidevaux, and S. D. Steenrod (2021), How Atmospheric Chemistry and Transport Drive Surface Variability of N2O and CFC-11, *J Geophys Res-Atmos*, *126*(8).

Schilt, A., M. Baumgartner, T. Blunier, J. Schwander, R. Spahni, H. Fischer, and T. F. Stocker (2010), Glacial-interglacial and millennial-scale variations in the atmospheric nitrous oxide concentration during the last 800,000 years, *Quaternary Sci Rev*, *29*(1-2), 182-192.

The pandas development team (2020), pandas-dev/pandas: Pandas, edited, Zenodo.

Thompson, R. L., et al. (2019), Acceleration of global N_2O emissions seen from two decades of atmospheric inversion, *Nature Climate Change*, *9*(12), 993-998.

Thompson, R. L., et al. (2014), TransCom N_2O model inter-comparison – Part 1: Assessing the influence of transport and surface fluxes on tropospheric N_2O variability, *Atmospheric Chemistry and Physics*, *14*(8), 4349-4368.

Tian, H. Q., et al. (2015), Global methane and nitrous oxide emissions from terrestrial ecosystems due to multiple environmental changes, *Ecosystem Health and Sustainability*, *1*(1), 1-20.

Tian, H., et al. (2019), Global soil nitrous oxide emissions since the preindustrial era estimated by an ensemble of terrestrial biosphere models: Magnitude, attribution, and uncertainty, *Global Change Biol*, *25*(2), 640-659.

Tian, H., et al. (2018), The Global N_2O Model Intercomparison Project, *B Am Meteorol Soc*, *99*(6), 1231-1252.

Tian, H, et al. (2020), A comprehensive quantification of global nitrous oxide sources and sinks, *Nature*, *586*(7828), 248-256.

Tian, H, et al. (2022), History of anthropogenic Nitrogen inputs (HaNi) to the terrestrial biosphere: a 5 arcmin resolution annual dataset from 1860 to 2019, *Earth System Science Data*, *14*(10), 4551-4568.

Van Rossum, G., and F. L. Drake Jr (1995), *Python tutorial*, Centrum voor Wiskunde en Informatica Amsterdam, The Netherlands.

Walker, A. P., et al. (2021), Integrating the evidence for a terrestrial carbon sink caused by increasing atmospheric CO2, *New Phytol*, *229*(5), 2413-2445.

Xu-Ri, and I. C. Prentice (2008), Terrestrial nitrogen cycle simulation with a dynamic global vegetation model, *Global Change Biol*, *14*(8), 1745-1764.

Xu, R. T., H. Q. Tian, S. F. Pan, S. R. S. Dangal, J. Chen, J. F. Chang, Y. L. Lu, U. M. Skiba, F. N. Tubiello, and B. W. Zhang (2019), Increased nitrogen enrichment and shifted patterns in the world's grassland: 1860-2016, *Earth System Science Data*, *11*(1), 175-187.

Yang, S., et al. (2020), Global reconstruction reduces the uncertainty of oceanic nitrous oxide emissions and reveals a vigorous seasonal cycle, *Proceedings of the National Academy of Sciences*, *117*(22), 11954-11960.